Received: 20 July 2023 | Revised: 31 August 2023 | Accepted: 5 September 2023

DOI: 10.1002/jcc.27231

RESEARCH ARTICLE

Journal of COMPUTATIONAL CHEMISTRY WILEY

Tuning ultrafast time-evolution of photo-induced charge-transfer states: A real-time electronic dynamics study in substituted indenotetracene derivatives

Luigi Crisci[1,2] | Federico Coppola[3] | Alessio Petrone[1,3,4] | Nadia Rega[1,3,4]

[1]Department of Chemical Sciences, University of Napoli Federico II, Complesso Universitario di M.S. Angelo, Naples, Italy

[2]Scuola Normale Superiore di Pisa, Pisa, Italy

[3]Scuola Superiore Meridionale, Naples, Italy

[4]Istituto Nazionale Di Fisica Nucleare, Sezione di Napoli, Complesso Universitario di M.S. Angelo ed. 6, Naples, Italy

Correspondence
Alessio Petrone and Nadia Rega, Department of Chemical Sciences, University of Napoli Federico II, Complesso Universitario di M.S. Angelo, via Cintia 21, I-80126, Naples, Italy.
Email: alessio.petrone@unina.it and nadia.rega@unina.it

Funding information
Gaussian; Ministero dell'Università e della Ricerca, Grant/Award Numbers: PRIN 2017YJMPZN001, PRIN 202082CE3T_002

Abstract

Photo-induced charge transfer (CT) states are pivotal in many technological and biological processes. A deeper knowledge of such states is mandatory for modeling the charge migration dynamics. Real-time time-dependent density functional theory (RT-TD-DFT) electronic dynamics simulations are employed to explicitly observe the electronic density time-evolution upon photo-excitation. Asymmetrically substituted indenotetracene molecules, given their potential application as n-type semiconductors in organic photovoltaic materials, are here investigated. Effects of substituents with different electron-donating characters are analyzed in terms of the overall electronic energy spacing and resulting ultrafast CT dynamics through linear response (LR-)TD-DFT and RT-TD-DFT based approaches. The combination of the computational techniques here employed provided direct access to the electronic density reorganization in time and to its spatial and rational representation in terms of molecular orbital occupation time evolution. Such results can be exploited to design peculiar directional charge dynamics, crucial when photoactive materials are used for light-harvesting applications.

KEYWORDS
electronic dynamics, indenotetracene, photo-induced charge-transfer, real-time TD-DFT, substituent effects

1 | INTRODUCTION

Charge transfer (CT), defined here as the phenomena where a fraction of charge is transferred between regions of space of the system,[1] has a crucial role in photosynthesis, biochemistry, and technological applications, such as generation and storage of electricity, photovoltaic cells, organic chromophores (i.e., light-emission diodes).[2-7] For these reasons it can be very useful to study the ultrafast fate of photo-induced states and, more specifically, the role of different functional groups on the chromophores on CT dynamics.[8-12] Thus, providing a molecular picture of the ultrafast (femto-second) dynamics among initial photo-excited states is pivotal for improving the efficiency of such devices.[13-16] The value of the electronic excitation energies can be not sufficient to the study above, and in fact, in practise for photo-induced charge-transfer states as well as for modeling the dynamics of a transferring electron in real time is required to explicit observe the electronic density evolving in time via electronic dynamics (ED) simulations.[17-22] Among non-perturbative approaches to mean-field quantum ED, real-time time-dependent density functional theory (RT-TD-DFT)[15,17,20,23-34] has been proven to be very powerful in these regards, since via real-time methods we can explicitly propagate in time the electronic density by evolving the time-dependent Schrödinger equation.

In particular, in this article, we focus on the capability of RT-TD-DFT in describing, simulating and interpreting on the molecular scale the ultrafast charge recombination, and more in general photo-

induced charge dynamics of photo-active molecules that have large potential in organic photovoltaic (OPV) applications. It is, indeed, necessary to acquire a deeper understanding of photo-induced ultrafast CT dynamics to have full control of the molecular processes underlying their functioning. OPV cells have several advantages since they are flexible, light, cheap and can be easily used for more adjustable devices.[35-37] Their peculiar and electronic properties derive from the possibility of using a very large range of differently functionalized molecules to modify the temporal evolution of the electronic charge and to simplify the modeling and the fine tuning of the: (i) electronic layout (i.e., the energy displacement and character of the electronic states), (ii) bad-gap, (iii) crystalline structure, (iv) solubility, (v) photo-stability. In recent years, research has put efforts to boost OPV performances by exploiting also the creation of multiexcitons (a bound coupled excited electron and an associated hole) generation from single photon absorption. A well-known photophysical process which typically occurs in crystalline materials,[38-44] known as singlet fission,[36,45,46] can come in handy in this field. Concerning the photophysical pathway, singlet fission is a spin-allowed phenomenon that involves at least two chromophoric units, but experimental and theoretical evidence concerning single molecules, such as carotenoids[47-50] and oligomers,[36,51-53] have been collected in the recent years.

The model systems investigated belong to the class of alternant hydrocarbons, promising as n-type compounds which can exploit photo-induced CT states to potentially undergo also singlet fission. We investigated photoinduced CT states of recently introduced asymmetrically substituted indenotetracene (ASI) molecules, which have been proposed to replace fullerene in OPV devices.[54,55] The cases study are two substituted diarylindenotetracene molecules bearing two methyls (2-Methyl-10-phenyl-9-(p-tolyl)indeno[1,2,3-fg]tetracene, namely Methyl ASI) or methoxy (2-Methoxy-9-(4-methoxyphenyl)-10-phenylindeno [1,2,3-fg]-tetracene, namely Methoxy ASI) substituent groups on both side of the indenotetracene scaffold, as reported in Figure 1. These systems have been previously synthesized and their optical absorption and electrochemistry have been characterized as well, as promising candidates for singlet fission applications.[54] In this context, the synergy between advanced spectroscopic techniques (time-resolved and non-linear)[56-61] and cutting-edge computational strategy can give the necessary tools to accurately understand the temporal evolution of electronic density and the relative structure-function interplay.[17-19,21,62-69] While in the actual device multiple monomeric units are arranged in a crystal or semi-crystal manner, the characterization of the excited states and their ultrafast dynamics in the monomeric units is the first mandatory and crucial step to understand CT dynamics in the ultrafast time scale of the photo-active material. In this respect, an accurate ab initio modeling strategy is required to understand the ultrafast photoinduced temporal evolution of the electronic density and to rationalize the effects induced by different functional groups.

To this aim, we first exploit linear response TD-DFT (LR-TD-DFT) formalism to characterize excitation energies and spacing among electronic levels (the electronic layouts). Then, to understand the ultrafast (subpicosecond) charge dynamics on the molecular scale, we rely on the non-perturbative mean-field quantum ED via real-time time-dependent density functional theory. RT-TD-DFT has been vastly employed in the past to model charge transfer and excitation dynamics directly and precisely in several donor-acceptor systems[15,17,64,70-72] and to provide the molecular interpretation of the interaction between initial photoexcited states,[16,17,34,63,73-76] exciton and polaron formation,[64,77-80] including relativistic effects.[81,82]

The nature of the energy shift for several electronic transitions was unveiled by correlating the electron-donor properties of the substituent with the spatial distribution of the molecular orbitals (MOs) and their dynamical involvement in the CT. Larger effects of the substituents were noticed in the electronic layout of the CT transitions, where the effect of the methoxy group resulting in a shifting of the charge transfer transition at lower energy values for the methoxy- if compared to the Methyl ASI. ED simulations revealed that is clear that the substituent has a role in the directionality of the recombination dynamics in the ultrafast regime (i.e., the Methoxy ASI shows a more complex and directional behavior while the methyl shows a quite symmetric rearrangement). Such results

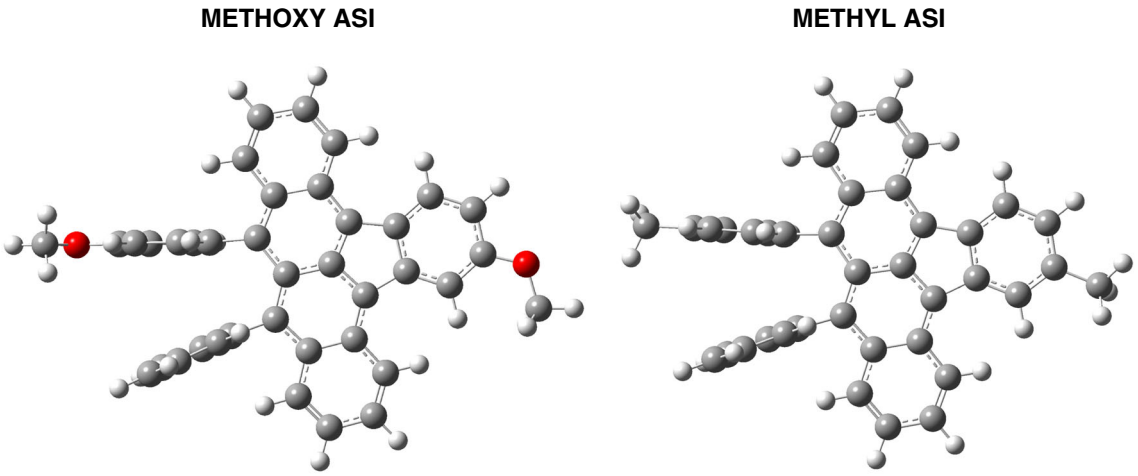

FIGURE 1 Ball and stick representations of the Methoxy ASI (left) and Methyl ASI (right) systems. Oxygen in red, hydrogen in white, and carbon in gray.

can be used as grounds to design peculiar photo-active materials, employed for light-harvesting applications.

2 | METHODOLOGY

The crystallographic structures of both Methoxy ASI and Methyl ASI were retrieved from Reference 54 and then atomic positions of the monomeric units were refined by gas-phase geometry optimization. Ground state energy, gradient and higher order properties were obtained within the DFT framework by solving the Kohn–Sham equation using the global hybrid Becke, 3-parameter, Lee-Yang-Parr (B3LYP) functional[83-89] and split valence double-ζ basis sets with additional polarization functions (6-31G(d,p)). DFT represents an appropriate alternative to explicit wavefunction methods,[90-96] as the desired balance between computational cost and accuracy can be achieved in large-scale systems.[60,97-109] Geometries were considered fully optimized when both the forces (maximum and root-mean-square [rms] force 0.000450 and 0.000300 Hartree/Bohr, respectively) and displacement (maximum and rms displacement 0.001800 and 0.001200 Bohr, respectively) values for all atoms were below the threshold criteria. The second derivatives of the energy with respect to the Cartesian nuclear coordinates were calculated to confirm that optimized geometries were local minima. All ground and linear response excited state computations are conducted using the electronic structure suite Gaussian16.[110]

2.1 | Excited state layout via linear response (LR-) TD-DFT

Vertical excitation energies and oscillator strengths are obtained by relying on methods rooted in time-dependent DFT in the linear response formalism (LR-TD-DFT),[23,25,30] using B3LYP with the Coulomb-attenuating approach (CAM-B3LYP) with 6-31g(d,p) basis set. CAM-B3LYP[111-116] is known to outperform canonical hybrid (i.e., B3LYP, PBE0, etc.) for the description of Rydberg-like and charge-transfer states, as some of the states of interest in this study, due to their high sensitivity to the treatment of exact exchange.[7,117-120] In this work, we focused on the first four singlet excited states for both the Methoxy ASI and Methyl ASI to better understand the role of the substituent on the most experimentally relevant transitions and the resulting electronic layout ruling the photophysics of these systems. This preliminary characterization is mandatory for investigating the photo-induced charge dynamics described by real-time ED, as explained in the following section.

2.2 | Ultrafast electronic dynamics via real-time (RT-)TD-DFT

The real-time time-dependent DFT approach to many-electron dynamics has been proven to be very powerful in describing, simulating, and interpreting on the molecular scale the ultrafast charge recombination and, more in general, photo-induced charge phenomena, since via real-time methods we can explicitly propagate in time the electronic density by evolving the time-dependent Schrödinger equation.[20,21] Herein, we present a brief description of the technique. Given an initial condition, the electronic density matrix is propagated according to the TD-DFT equation, reported here, in atomic units.

$$i\frac{d\mathbf{P}(t)}{dt} = [\mathbf{K}(t), \mathbf{P}(t)], \tag{1}$$

where **P** and **K** are density and Kohn–Sham matrices on an orthonormal basis. By the use of a modified midpoint unitary transformation algorithm,[74,121] Equation (1) is numerically integrated. The density matrix is propagated by exploiting a unitary time evolution operator, $U(t_n)$

$$\mathbf{P}(t_{n+1}) = \mathbf{U}(t_n) \cdot \mathbf{P}(t_{n-1}) \cdot \mathbf{U}^{\dagger}(t_n), \tag{2}$$

to obtain the time evolution operator, given a time step as Δt:

$$\mathbf{U}(t_n) = \exp[-i \cdot 2\Delta t \cdot \mathbf{K}(t_n)] = \mathbf{C}(t_n) \cdot \exp[-i \cdot 2\Delta t \cdot \epsilon(t_n)] \cdot \mathbf{C}^{\dagger}(t_n), \tag{3}$$

where eigenvectors $C(t_n)$ and eigenvalues $\epsilon(t_n)$ are retrieved from the Kohn–Sham matrix at time t_n. It must be emphasized that, since the nature of the wavefunction is precisely a superposition of relevant many-body states of the system like that observed immediately after the photo absorption, this dynamics is representative of the motion of a localized wave packet in a symplectic electronic parameter phase space.[121]

Since we are interested in the low-lying optically accessible states, we first characterize the Methoxy ASI and Methyl ASI electronic layout by performing LR-TD-DFT calculations, as discussed in the result section. To perform RT-TD-DFT ED, the initial electronic density to propagate is prepared, promoting an electron from a selected occupied MO to an unoccupied one ("Koopman excitation"—orbital population swap) according to the electronic transition of interest between the singlet ground state (S_0) and the *n*th singlet excited state (S_n), whose main orbital contributions are resolved using preliminary frequency domain LR-TD-DFT calculations. According to a well-established procedure, the "Koopman excitation" step creates a non-stationary electron density that is representative of a coherent superposition of the ground and excited states of interest.[21,62,64,80,122] Since we are not allowing the nuclei to move (fixed nuclei approximation, by starting from a minimum geometry), this procedure can be used as a reasonable approximation of a vertical excitation in the Franck–Condon region in the ultrafast regime ($\lesssim$ 50 fs). In such short simulated time, indeed, it could be assumed that the effect of nuclear vibrations is still limited. Therefore, the "fixed nuclei" approximation implied in these purely ED is reasonable. To better characterize the excited state time evolution, the electronic density in orthonormal basis is transformed back in atomic orbital (AO) basis by the Löwdin scheme, and the time-dependent density in this AO basis, $\mathbf{P}'(t)$, is projected into the ground state MO space giving:

$$n_i(t) = \mathbf{C}_i'^{\dagger}(0)\mathbf{P}'(t)\mathbf{C}_i'(0), \quad (4)$$

where n_i is the effective occupation number of the ground state orbital $\mathbf{C}_i'(0)$ in the AO basis. The time-dependent dipole moment $\mu(t)$ is also computed at each step from the following:

$$\mu(t) = Tr\,[\mathbf{D}'\mathbf{P}'(t)], \quad (5)$$

where **D'** is the electric dipole momentum operator in AO basis. A 1.0 attosecond time step was used when integrating the TD-DFT equation of motion. All RT-TD-DFT calculations were performed with the same level of theory of LR-TD-DFT computations and employing a modified development version of Gaussian.[123]

3 | RESULTS AND DISCUSSION

3.1 | Electronic layout characterization

In the present work, the characterization of the low-lying electronic transitions via LR-TD-DFT calculations has been extended beyond the S_1 state (this last one was studied in details in Reference 54) by analyzing the higher energy singlet transitions to locate the lowest energy CT states. Thus, the effects of different substituents on the electronic layout and, above all, on higher energy states (important for photo-induced charge-dynamics) of the indenotetracene scaffold can be better understood. Table 1 summarizes the results computed for both Methoxy ASI and Methyl ASI substituted systems. The first electronic transition is optically allowed for both ASI dyes and are computed at 2.41 and 2.44 eV for Methoxy ASI and Methyl ASI compounds, respectively, in nice agreement with previous experimental and theoretical findings by Cramer and coworkers.[54] We observed a moderate red-shift for the $S_1 \leftarrow S_0$ transition of −0.03 eV from Methyl ASI to Methoxy ASI, in accordance with Reference 54 and a larger one (−0.12 eV) for the $S_2 \leftarrow S_0$ transition. Contour plots of MOs that mainly contribute to the first two transitions (see Table 1 for MOs contributions) are reported under Figure 2 showing a non-negligible electronic density distribution in the proximity of the different peripheral substituent groups for both the Methyl ASI and Methoxy ASI compounds.

In particular, from Figure 2 we underlie that the $S_1 \leftarrow S_0$ presents a similar alternating bond (AB) nature for both systems (as observed in Reference 54), explaining also the similar values computed for the oscillator strength (from Table 1 a difference of Δf=0.024 is observed), resulting in the bright character of these transitions for both (oscillator strengths of 0.254 and 0.278, for the Methoxy ASI and Methyl ASI, respectively). For the $S_2 \leftarrow S_0$ transition, the Methoxy ASI presents a slightly marked intramolecular CT character while an alternating bond character is preserved for the Methyl ASI. These transitions are slightly allowed (f=0.032) and dark (f=0.006) for Methoxy ASI and Methyl ASI, respectively, although a similar difference in oscillator strengths, as for the previous case, is registered (Δf=0.026). We now analyze the main differences in terms of MOs isosurfaces to emphasize the role of the substituents on the aforementioned transitions. First, a very close electronic density distribution is observed for both Methoxy ASI and Methyl ASI LUMOs. Consequently, the origin of the red-shift for the methoxy derivative requires the comparison of the HOMO and the HOMO-1 respectively for $S_1 \leftarrow S_0$ and the $S_2 \leftarrow S_0$ transitions. For the S_1 case, the main difference between the two HOMOs regards a larger electronic density rearrangement on the substituent group for the Methoxy ASI with respect to the Methyl ASI. Since methoxy is a better electron-donor group and HOMO has a non-negligible isodensity on this moiety (while the LUMO has an almost null contribution on it), we can say that this tendency leans toward destabilizing the HOMO more for the Methoxy ASI with the subsequent larger decrease in the HOMO-LUMO energy gap, resulting in the observed red-shift. Such findings are in perfect agreement with the similar trend observed trough cyclic voltammetry measurements.[54] The $S_2 \leftarrow S_0$ transition involves the HOMO-1 that shows a different nature for the Methyl ASI case, where it is more delocalized also on the entire indenotetracene scaffold as in the LUMO, while for the Methoxy ASI, the substituent region plays a larger role in percentage. Such a difference can explain (i) the different nature of these transitions, still alternating bond for Methyl ASI (as for the first one) and CT for Methoxy ASI (different from the first one), (ii) the larger red-shift observed with respect to the $S_1 \leftarrow S_0$, given the HOMO-1 of

TABLE 1 LR-TD-CAM-B3LYP/6-31G(d,p) vertical excitation energy values (eV) and the frontier orbitals that mostly contribute (*h* states for HOMO and *l* for LUMO) for the first four low-lying electronic transitions of the *Methoxy ASI* (left) and *Methyl ASI* (right).

State	Methoxy ASI					Methyl ASI				
	ΔE	f	χ		Allowed	ΔE	f	χ		Allowed
S_1	2.41	0.254	AB	$h \rightarrow l$	Yes	2.44	0.278	AB	$h \rightarrow l$	Yes
S_2	2.67	0.032	CT	$h-1 \rightarrow l$	Slightly	2.79	0.006	AB	$h-1 \rightarrow l$	No
S_3	3.53	0.069	CT	$h-3 \rightarrow l$	Slightly	3.54	0.073	CT	$h-3 \rightarrow l$	Slightly
S_4	3.66	0.005	CT	$h-2 \rightarrow l$	No	3.91	0.0002	CT	$h-2 \rightarrow l$	No

Note: Oscillator strengths are reported in parentheses. The transition character is indicated in the χ column where AB stands for alternating bond and CT for charge transfer. In the last column we define if the transitions are predicted to be allowed (yes, $f > 0.1$), dark (no, $f < 0.01$), or slightly active (slightly, $0.01 < f < 0.1$).

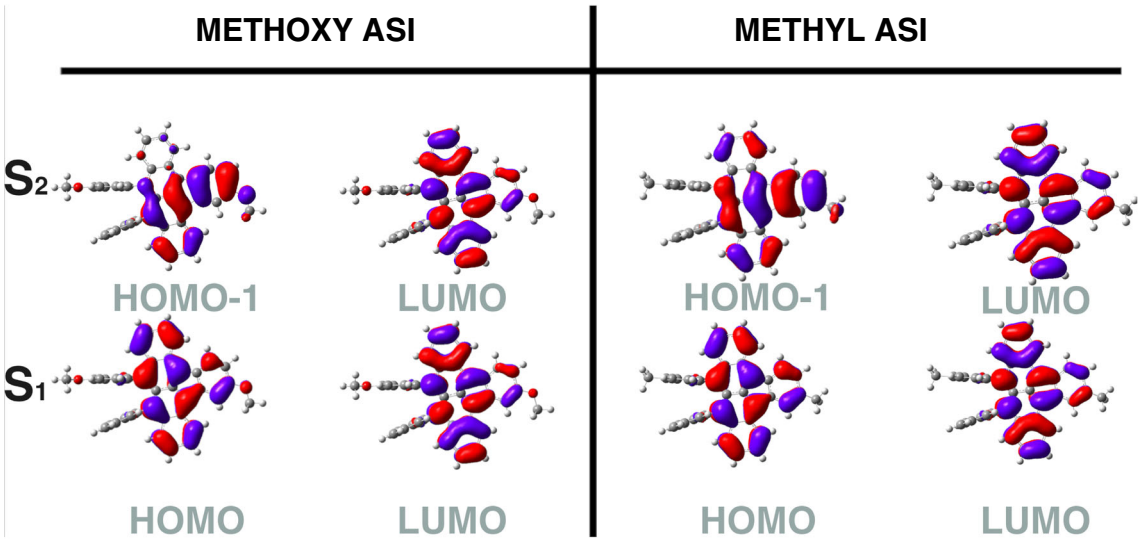

FIGURE 2 *CAM-B3LYP*/6-31G(d,p) isosurfaces (isovalue = 0.02) of the frontier MOs mainly responsible (see Table 1) in the $S_2 \leftarrow S_0$ (top) and $S_1 \leftarrow S_0$ (bottom) transitions of Methoxy ASI (left) and Methyl ASI (right).

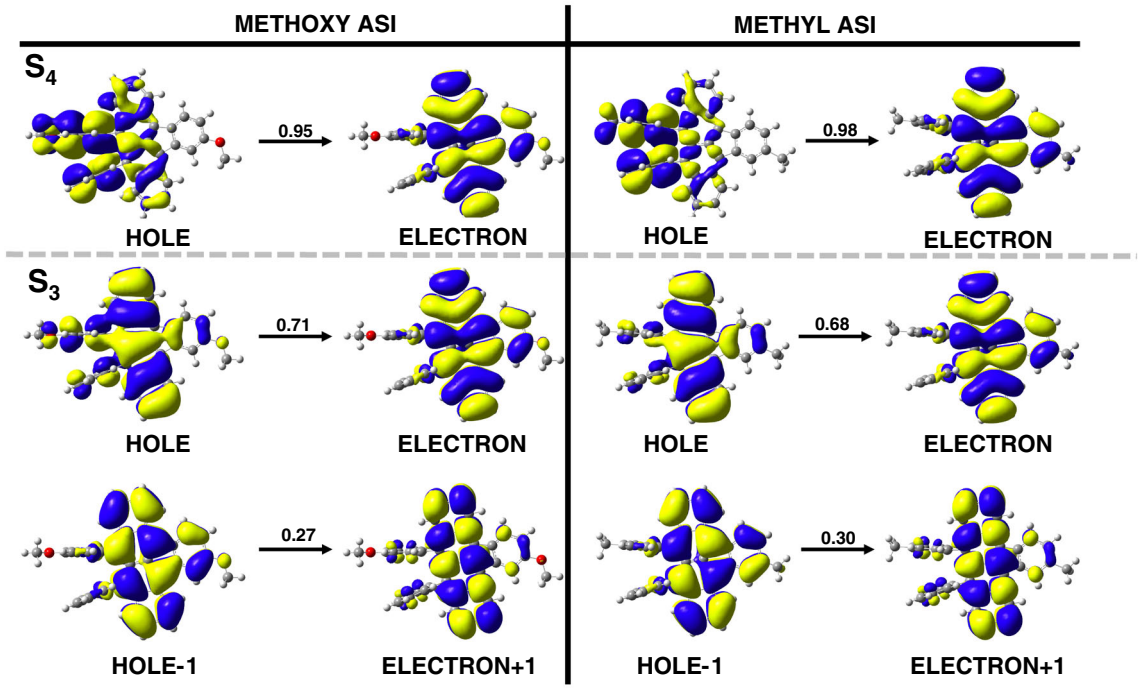

FIGURE 3 Isosurface (isovalue = 0.01) of NTOs. Hole/hole-1 and electron/electron+1 pairs for the $S_3 \leftarrow S_0$ (bottom) and $S_4 \leftarrow S_0$ (top) transitions calculated at the *TD-CAM-B3LYP*/6-31G(d,p) level of theory are reported for the Methoxy ASI (left) and Methyl ASI (right). The contribution to the transition of each NTO pair is shown on top of each arrow connecting them.

Methoxy ASI more localized in percentage on an electron-donating substituent; (iii) the dissimilarity in transitions brightness, given that the Methoxy ASI HOMO-1 has a different symmetry of the Methyl ASI HOMO-1, slightly allowing $S_2 \leftarrow S_0$ transition in the first case.

Now we move to the higher energy transitions. For both $S_3 \leftarrow S_0$ and $S_4 \leftarrow S_0$, multiple pairs of canonical MOs with comparable CI coefficients participate in defining the nature of these transitions. To provide an easier molecular picture, we computed natural transition orbitals (NTOs)[124] which have proved useful to better analyze and visualize the electronic redistribution in such cases in terms of a reduced number of *hole-electron* pairs (see Figure 3).[65,66,125] A close inspection of Figure 3 reveals several differences between the starting hole NTOs for Methoxy ASI and Methyl ASI regarding both electronic transitions, showing interesting features due to the different involvements of the alkoxy and alkyl substituents, while negligible differences between the electron NTOs are observed, instead. Fort both Methoxy

ASI and Methyl ASI, the $S_3 \leftarrow S_0$ transition can be considered slightly allowed (f=0.069 and 0.073, respectively) and almost similar in excitation energy (−0.01 eV from Methyl ASI to Methoxy ASI), their character can be expressed by two very similar *hole-electron*NTOs pairs (see Figure 3, bottom panel). Regarding the NTO pair with the highest contribution (∼0.7), in both cases, the *hole* is delocalized along the entire indenotetracene scaffold with a non-negligible contribution of all peripheral phenyl rings and oxygen lone pairs (both the sides of the scaffold). The *electron* NTO, instead, is less symmetrically distributed on the phenyl rings, thus, suggesting a CT nature for $S_3 \leftarrow S_0$ transition (from left to right in the figure) for both systems. In both cases, the *hole-1 electron+1* pair (contribution to the transition ∼0.3) can be described by an alternating bond redistribution.

The $S_4 \leftarrow S_0$ transition can be conveniently represented by a single NTO pair (contribution to the transition close to 1.00) for both systems. This time in both derivatives the transition probability is very low (f < 0.001) and a marked red-shift of −0.25 eV is observed from the Methyl ASI to Methoxy ASI. In both cases, the *hole* is asymmetrically localized on one side of the system (mostly the two phenyl substituent groups on the left in Figure 3 and partially on the tetracene portion). Upon excitation, the density reorganizes towards the indenotetracene moiety (*electron*), revealing a strong CT character for this state. From this analysis, it is clear that the substituent plays a larger role in this transition, explaining the larger red-shift observed this time, since methoxy is a better electron-donor group and can more destabilize the hole. One interesting result is the role of different substituents in inducing changes to the indenotetracene electronic layout. In particular, the substituent nature can affect the order of the first charge transfer transition, which is observed in the $S_3 \leftarrow S_0$ in the case of Methyl ASI while is the $S_2 \leftarrow S_0$ for the Methoxy ASI.

Similar substituent modulation of the electronic properties for other highly conjugated molecular systems used as dyes in dye-sensitized solar cells, mainly π linkers in triphenylamine, has also been predicted in previous studies.[126] To have a deeper understanding of ultrafast CT dynamics we will examine the charge recombination dynamics through RT-TD-DFT electron dynamics and by focusing on the first optically active CT transitions just discussed, namely, the $S_2 \leftarrow S_0$ for the Methoxy ASI and the $S_3 \leftarrow S_0$ for the Methyl ASI, respectively.

3.2 | Electronic tuning effects of methyl and methoxy groups

Before moving to CT dynamics, we elucidate the relationship between the electron-donating ability of methyl and methoxy groups on the energy of MOs involved in the electronic transition reported in Table 1, please see Figure 4. The MOs eigenvalues of the two ASI dyes are compared to the unsubstituted homologue and are reported, along with their isodensity representations, in Table S1 and in Figure S1, respectively.

Concerning the $S_1 \leftarrow S_0$ transition, by direct comparison, the LUMO is more energetic than the non-substituted indenotetracene (0.07 eV for Methoxy ASI and 0.06 eV for Methyl ASI). The same energy difference (0.01 eV) is observed for the HOMO of methoxy- and methyl-functionalized derivatives, which are, respectively, 0.08 and 0.07 eV above the HOMO of the unsubstituted molecule (−5.99 eV). The patterns found, in agreement with previous theoretical and experimental results,[54] are directly comparable with the orbital contours presented in Figure S1, which show to have similar contributions on the same atoms. We investigated the energetic alignment of the occupied orbitals just below HOMO given their crucial importance for photo-induce CT dynamics. It is important to underline that the occupied orbitals at lower energy present more marked energetic differences and better emphasize the degree of electron donation of the two substituents.

The HOMO-1 of Methoxy ASI and Methyl ASI is 0.31 and 0.11 eV above the orbital of the non-substituted indenotetracene (−6.85 eV). Consequently, the observed redshift for the $S_2 \leftarrow S_0$ transition (0.12 eV) can be explained by assuming that the *p*-methoxyphenyl group provides electron density only to a portion of the indenotetracene, leading to a slight energetic destabilization of HOMO-1 since it is not completely delocalized as in the case of Methyl ASI.

Concerning HOMO-2 for diarylindenotetracene, the electronic density is distributed between the peripheral phenyl rings and the tetracene core (left panel of Figure S1), whereas for the two derivatives, the tetracene is less involved (central and right panels of Figure S1 in ESI). The higher degree of electron donation of the alkoxy group leads to a significant increase in energy (0.51 eV) compared to the Methyl ASI case (0.14 eV) and to the non-functionalized indenotetracene, whose HOMO-2 is at −7.60 eV. The negligible red-shift computed for the $S_3 \leftarrow S_0$ transition (0.01 eV) is in agreement if it is considered that the arrival electronic state is severely combined with other orbital pairs (see CI coefficients in Table S1), including LUMO+1 and LUMO +2 located at 0.57 and 0.75 eV for Methoxy ASI and 0.53 and 0.74 eV for Methyl ASI that thus align the resultant energy gaps.

Two orbital pairs, HOMO-2-LUMO and HOMO-3-LUMO, characterize the nature of the $S_4 \leftarrow S_0$ electronic transition. Since for Methoxy ASI and Methyl ASI the isodensity of the target orbital is very similar, the observed red-shift (0.25 eV) may result from the mixing of HOMO-2 and HOMO-3 which have different energies. Specifically, for the HOMO-3 of the methyl derivative the electron density on the ring containing the $-CH_3$ group is responsible for the lower energy increase (0.02 eV) with respect to the Methoxy ASI case (−7.66 eV) for which the electronic density is mainly confined on the tetracene moiety. Given that materials based on photoactive indenotetracene scaffolds are also promising for photovoltaic devices in the field of solar cells, a detailed comprehension of the ultrafast photo-induced charge transfer dynamics on the molecular scale represent a key element for the development of improved materials to boost novel technological applications (Figure 4).

3.3 | Real-time TD-DFT electronic dynamics

Initial conditions for resembling the CT electronic transitions of interest are prepared according to the orbital swap procedure explained in

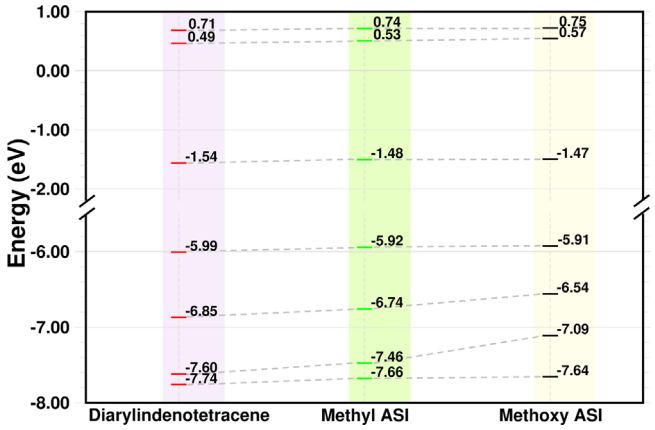

FIGURE 4 From left to right: Diarylindenotetracene, Methyl ASI and Methoxy ASI canonical molecular orbitals eigenvalues (in eV) from HOMO-3 to LUMO+2 in increasing order of energy, computed at CAM-B3LYP/6-31G(d,p) level of theory. The MO isodensity representations are reported in Figure S1.

the methods and by exploiting the results of the previous sections. We focused here, given their potential role in light harvesting phenomena, on the lowest (in energy) charge transfer transitions from the ground to the S_3 for the Methyl ASI (initial state prepared as HOMO-3 to LUMO swap) and the S_2 for the Methoxy ASI (initial state prepared as HOMO-1 to LUMO swap) (see Table 1). We first analyze in Figure 5 the ultrafast (≤ 20 fs) dynamics by monitoring the electronic dipole time evolution (along with its Cartesian components) to better understand the charge dynamics on the system and the interconnected role of different substituents. The Methoxy ASI has a large change in the dipole values upon excitation. This is expected given the nature of the involved MOs and the CT transfer character of the excitation. Such a charge reorganization can be seen by inspecting the initial change (t_0, right after the orbital swap) in the value of the total dipole with respect to S_0 (μ_{Tot} (t_0) = 8.32 D, $\Delta\mu_{Tot} \sim$ 5.5 D; ground state dipole components, before the swap, are: μ_x (S_0) = −2.10 D, μ_y (S_0) = −1.55 D, μ_z (S_0) = −1.01 D; μ_{Tot} (S_0) = 2.80 D) and it is initially mostly along the *x* direction (μ_x (t_0) = −8.16 D). The CT can be analyzed in space by monitoring the dipole component dynamics, and we can observe an initial CT mostly located in the plane of the indenotetracene scaffold but in the direction orthogonal to the major axis of such moiety and thus connecting the substituent rings on the opposite sides (see top left panel in Figure 5, for axis representation). Then, as soon the electronic density evolves in time, the *x* component of electric dipole moment (black line in the top panel of Figure 5) shows immediately larger and larger oscillations, reaching its maximum value after ∼10 fs ($\mu_x \sim$ 5 D). These large amplitude oscillations are present for the entire ED until the end, but around a lower final average value ($\mu_x \sim$ 1.2 D). In contrast, the *y* component starts from a value similar to the ground state (μ_y (t_0) ∼ −1.5 D) and we observe small oscillations until ∼ 10 fs of this component. After 10 fs, large amplitude oscillations are present also for μ_y, as for the *x* component, and its final average value decreases, although in a smaller magnitude with respect to the final *x* one (final $\mu_y \sim -1$ D). There is no interesting dynamics along the *z* dipole component that shows a constant value equal to the unperturbed system in its ground state, indicating no net out-of-plane electronic density rearrangement. From these trends, we can deduce an electronic density reorganization in 20 fs that starts mostly along the direction connecting the substituent of the indenotetracene scaffold, evolving through the substituted phenyl groups (*x* component) and after 10 fs, such dynamics is perturbed by the additional oscillation of the charge from the bottom to the top of the major axis of the indenotetracene scaffold (*y* component). Indeed, from such analysis, we can tell that the Methoxy ASI ED clearly indicates an important CT that might involve multiple orbitals, given the different nature and timings of the oscillations affecting the *x* and *y* components (see following MO occupation analysis).

The Methyl ASI dipole dynamics shows a significant CT character, although slightly smaller with respect to the previous case (μ_{Tot} (t_0)= 5.51 D, $\Delta\mu_{Tot} \sim$ 4 D; ground state dipole components, before the swap, are: μ_x (S_0) = 1.57 D, μ_y (S_0) = −0.33 D, μ_z (S_0) = 0.07 D; μ_{Tot} (S_0) = 1.60 D). The major dynamics starts with an electronic density reorganization involving only the direction orthogonal to the indenotetracene scaffold, evolving through the substituted phenyl groups (*x* direction, see Figure 5 for axis representation) (μ_x (t_0) = 5.50 D). Then, such a *x* component shows both a high and a low-frequency oscillation in its dynamics, reaching a maximum value around ∼6 fs ($\mu_x \sim$ 7.5 D) with a resulting larger period of ∼12 fs. In this case, the data analysis is simplified by the fact that the *z* and *y* axis oscillates around ∼0 D, indicating no net displacement outside the indenotetracene scaffold plane and along its major axis during the ED.

During the electronic density evolution, monitored via the dipole analysis, we note for both Methoxy ASI and Methyl ASI systems a charge reorganization that affects the indenotetracene scaffold and the spatial region connecting the phenyl groups. Comparing the electric dipole moment time evolution between the two monomers, we record that the Methyl ASI does not show significant charge dynamics in other regions while the Methoxy ASI seems to have a more complex behavior, involving an additional component along the major axis of such a scaffold (along the *y* direction). Several useful information regarding the photoinduced charge separation can be deduced from the trend of the total dipole moment and its respective components. However, a detailed molecular and spatial picture can be obtained only by a closer look at the MOs that play the larger role in the electronic density reorganization in time upon excitation and thus from the analysis of the MO occupation number dynamics reported in Figure 6.

In the case of the Methoxy ASI monomer (Figure 6, left), we observe a crossing point in the orbital population around 8 fs, where the initial populated LUMO loses ∼50% of its initial value. After 12 fs, the HOMO-1 population seems to be recovered, although the HOMO starts to be depopulated, instead. After 15 fs, until the end, both HOMO and HOMO-1 are still involved in exchanging ∼20% of the population. It is interesting to note what happens at about ∼12.5 fs. From the trend of the occupation numbers, it is possible to see a switch between the most occupied orbitals leading to a more

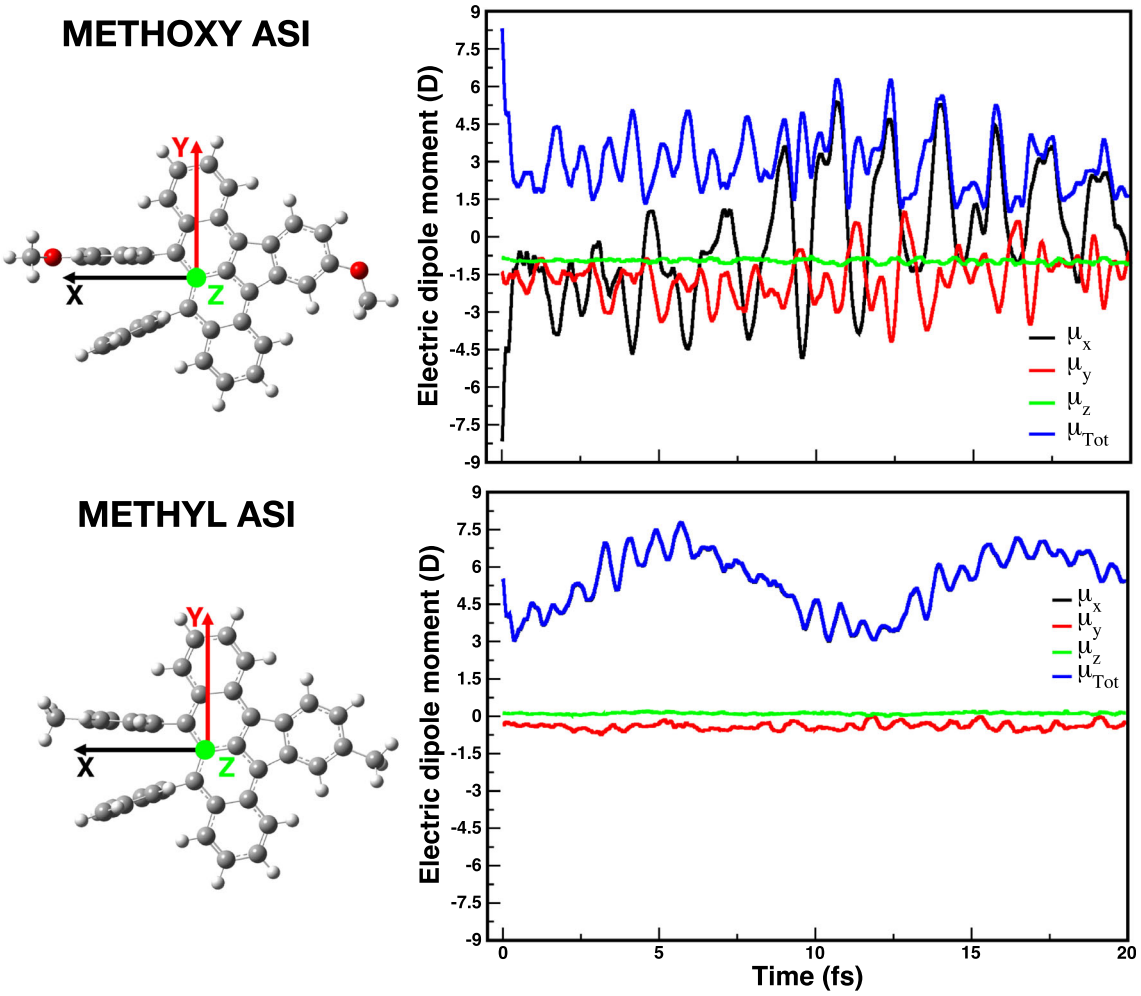

FIGURE 5 Time resolved electric dipole moment (total and *x*,*y*,*z* components) obtained by RT-TD-CAM-B3LYP/6-31G(d,p) electronic dynamics, where initial conditions resemble the $S_3 \leftarrow S_0$ (Methyl ASI, top panel) or the $S_2 \leftarrow S_0$ (Methoxy ASI, bottom panel) transition. In the case of the Methyl ASI the total electric dipole moment and its *x* component are superimposed. Ball and stick representations of the corresponding Methyl ASI and Methoxy ASI structures are reported on the left for convenience along with axis orientations: *x* axis is oriented in the direction of the two phenyls substituent groups, the *z* axis is perpendicular to the molecule's plane, and the *y* axis is along the major axis of the indenotetracene scaffold.

populated HOMO with respect to the HOMO-1. This situation corresponds to a charge shift toward positive values along the *y*-axis. In the same time interval, we can also observe the maximum value of the *y* component of the dipole moment. This occupation number dynamics explains both the charge oscillations and the resulting charge separation along both the *x* and *y* directions of the molecule, observed in Figure 5. Indeed, HOMO-1, HOMO and LUMO are located along the direction connecting the phenyl substituents (*x* direction). Moreover, the HOMO-1 has a not symmetric density along the major indenotetracene scaffold axis (*y* direction), explaining the additional charge dynamics along such a direction, which is absent in the Methyl ASI (see following discussion).

For the second derivative (Methyl ASI Figure 6, right), a MO population recombination dynamics is observed, where the first crossing between the occupation of the LUMO and the depleted HOMO-3 occurs around ∼3 fs (faster than the previous case), with the HOMO-3 occupation number reaching its maximum value at 6 fs. We have seen that in the first 6 fs the component of the μ_x increased until it reached the maximum value of ∼7.5 D as well, showing again that the dipole can be correlated to the MO occupation dynamics. After that a decrease of the HOMO-3 population is observed and the LUMO gains back full population at ∼12 fs. Then, the density starts oscillating back and forth between the two orbitals with a period of ∼12 fs. This population oscillation mirrors the trend in the corresponding dipole dynamics, where the same period can be seen in the time evolution of the *x* dipole component (see Figure 5). From this analysis is clear why in the Methyl ASI the charge recombines mostly along the *x* direction, due to the spatial distribution of the HOMO-3 and LUMO, asymmetric along the direction connecting the phenyl substituents (*x* direction) and symmetrically distributed along the major axis of the indenotetracene scaffold (*y* direction). Indeed, by a closer look at the involved MOs during the transition (see Figure 6,

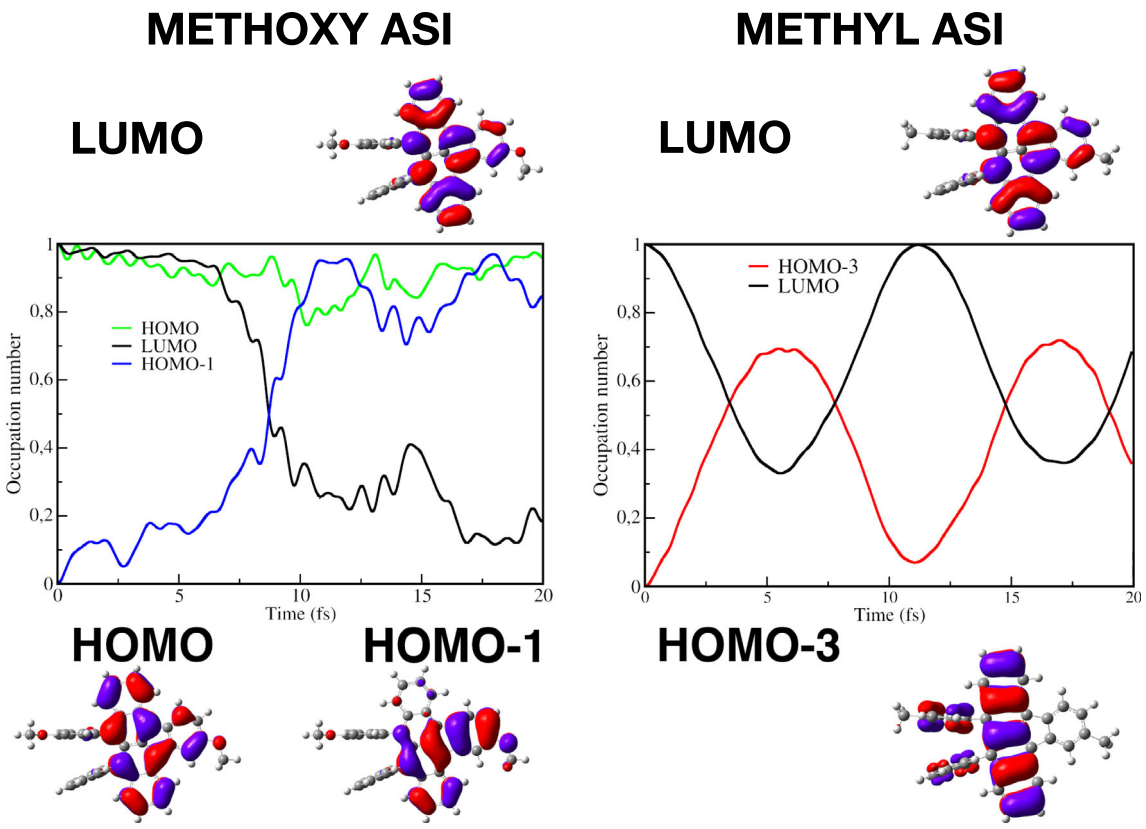

FIGURE 6 Time resolved molecular orbital occupation number obtained by a 20 fs RT-TD-CAM-B3LYP/6-31G(d,p) electronic dynamics, where initial conditions resemble the $S_2 \leftarrow S_0$ transition by a HOMO-1 to LUMO occupation swap (Methoxy ASI, left) and the $S_3 \leftarrow S_0$ transition obtained by a HOMO-3 to LUMO occupation swap (Methyl ASI, right). Isodensity plots of the most involved MOs are also reported.

right side), it is clear that the MO swap does not lead to net reorganization along the *y*-axis. This behavior in the Methyl ASI is reflected in the null *y* electric dipole moment component evolution (see Figure 5) and the observed dynamics of the *x* component. At variance, in the Methoxy ASI significant dynamics of both *y* and *x* components were observed.

In summary, the Methoxy ASI appears to have a multi-directional charge transfer dynamics while the Methyl ASI privileges the direction orthogonal to the indenotetracene scaffold and connecting the phenyl substituents (*x* direction in Figure 5). These results can be obtained only by directly observing the ED via RT simulations. This technique can provide direct access to the electronic density reorganization in time and to its spatial and rational representation in terms of MO occupation time evolution, indeed.

4 | CONCLUSIONS

A comprehensive study of photo-induced charge-transfer states as well as the dynamics of a transferring electron in time has been conducted. Via real-time time-dependent density functional theory ED, a molecular picture of the ultrafast (femto-second) dynamics of CT states has been unrevealed to enhance the efficiency of photo-active devices based on organic photovoltaic materials. In this work we studied the class of asymmetrically substituted indenotetracene molecules and effects of substituents with different electron-donating characters are investigated on both the overall electronic energy spacing and resulting ultrafast CT dynamics by employing both LR-TD-DFT and RT-TD-DFT based approaches. A red-shift in the vertical excitation energies of the methoxy-substituted derivative with respect to the methyl-substituted one was observed, showing the capability of different substituent groups in tuning the electronic layout and the resulting optical absorption. For each transition, the nature of the energy shift was unveiled by correlating the electron-donor properties of the substituent with the spatial distribution of the canonical MOs (or NTOs) involved. Larger effects of the substituents were noticed in the electronic layout of the charge transfer transitions, where the effect of the methoxy group resulting in a shifting of the charge transfer transition at lower energy values for the methoxy- if compared to the Methyl ASI. ED simulations allowed us to look closely at the electronic density evolution in terms of the electric dipole moment and the MO occupation evolution. In particular it is evident that the substituent has a role in the directionality of the recombination dynamics in the ultrafast regime (i.e., the Methoxy ASI shows a more complex and directional behavior while the methyl shows a quite symmetric rearrangement). Such results can be exploited to design peculiar directional charge dynamics, very important when photo-active materials are employed for light-harvesting applications.

ACKNOWLEDGMENTS

Authors thank Gaussian Inc. and the Italian Ministry of University and Research (Projects: PRIN 2017YJMPZN001, PRIN 202082CE3T_002) for financial support.

CONFLICT OF INTEREST STATEMENT

There are no conflicts to declare.

DATA AVAILABILITY STATEMENT

The data that support the findings of this study are available from the corresponding author upon reasonable request.

ORCID

Luigi Crisci https://orcid.org/0000-0002-8140-5397
Federico Coppola https://orcid.org/0000-0002-5845-4211
Alessio Petrone https://orcid.org/0000-0003-2232-9934
Nadia Rega https://orcid.org/0000-0002-2983-766X

REFERENCES

[1] A. D. McNaught, A. Wilkinson, *Compendium of Chemical Terminology*. IUPAC Nomenclature Books Series, 2nd ed., Blackwell Science, Hoboken, NJ **1997**.
[2] G. D. Scholes, G. R. Fleming, A. Olaya-Castro, R. Van Grondelle, *Nat. Chem.* **2011**, *3*, 763.
[3] S. Kundu, A. Patra, *Chem. Rev.* **2017**, *117*, 712.
[4] G. J. Hedley, A. Ruseckas, I. D. Samuel, *Chem. Rev.* **2017**, *117*, 796.
[5] J. Chen, A. Schmitz, T. Inerbaev, Q. Meng, S. Kilina, S. Tretiak, D. S. Kilin, *J. Phys. Chem. Lett.* **2013**, *4*, 2906.
[6] S. Kilina, P. Cui, S. A. Fischer, S. Tretiak, *J. Phys. Chem. Lett.* **2014**, *5*, 3565.
[7] G. García, C. Adamo, I. Ciofini, *Phys. Chem. Chem. Phys.* **2013**, *15*, 20210.
[8] J. P. Zobel, L. González, *JACS Au* **2021**, *1*, 1116.
[9] F. Talotta, M. Boggio-Pasqua, L. González, *Chem. - Eur. J.* **2020**, *26*, 11522.
[10] F. Perrella, A. Petrone, N. Rega, *J. Chem. Theory Comput.* **2023**, *19*, 626.
[11] F. Perrella, F. Coppola, N. Rega, A. Petrone, *Molecules* **2023**, *28*, 3411.
[12] F. Perrella, A. Petrone, N. Rega, *Phys. Chem. Chem. Phys.* **2021**, *23*, 22885.
[13] C. Daniel, *Phys. Chem. Chem. Phys.* **2021**, *23*, 43.
[14] J. Eng, C. Gourlaouen, E. Gindensperger, C. Daniel, *Acc. Chem. Res.* **2015**, *48*, 809.
[15] U. De Giovannini, G. Brunetto, A. Castro, J. Walkenhorst, A. Rubio, *ChemPhysChem* **2013**, *14*, 1363.
[16] M. A. Marques, A. Castro, G. F. Bertsch, A. Rubio, *Comput. Phys. Commun.* **2003**, *151*, 60.
[17] K. Lopata, N. Govind, *J. Chem. Theory Comput.* **2011**, *7*, 1344.
[18] D. R. Nascimento, A. E. DePrince III, *J. Chem. Theory Comput.* **2016**, *12*, 5834.
[19] M. A. Marques, X. López, D. Varsano, A. Castro, A. Rubio, *Phys. Rev. Lett.* **2003**, *90*, 258101.
[20] X. Li, N. Govind, C. Isborn, A. E. DePrince III, K. Lopata, *Chem. Rev.* **2020**, *120*, 9951.
[21] J. J. Goings, P. J. Lestrange, X. Li, *Wiley Interdiscip. Rev.: Comput. Mol. Sci.* **2018**, *8*, e1341.
[22] N. T. Maitra, *J. Phys.: Condens. Matter* **2017**, *29*, 423001.
[23] M. E. Casida, *Recent Advances in Density Functional Methods: (Part I)*, World Scientific, Singapore **1995**, p. 155.
[24] C. Van Caillie, R. D. Amos, *Chem. Phys. Lett.* **2000**, *317*, 159.
[25] A. Dreuw, M. Head-Gordon, *Chem. Rev.* **2005**, *105*, 4009.
[26] R. E. Stratmann, G. E. Scuseria, M. J. Frisch, *J. Chem. Phys.* **1998**, *109*, 8218.
[27] M. Petersilka, U. Gossmann, E. Gross, *Phys. Rev. Lett.* **1996**, *76*, 1212.
[28] G. Scalmani, M. J. Frisch, B. Mennucci, J. Tomasi, R. Cammi, V. Barone, *J. Chem. Phys.* **2006**, *124*, 094107.
[29] R. Bauernschmitt, R. Ahlrichs, *Chem. Phys. Lett.* **1996**, *256*, 454.
[30] M. E. Casida, C. Jamorski, K. C. Casida, D. R. Salahub, *J. Chem. Phys.* **1998**, *108*, 4439.
[31] S. A. Fischer, C. J. Cramer, N. Govind, *J. Chem. Theory Comput.* **2015**, *11*, 4294.
[32] A. Bruner, S. Hernandez, F. Mauger, P. M. Abanador, D. J. LaMaster, M. B. Gaarde, K. J. Schafer, K. Lopata, *J. Phys. Chem. Lett.* **2017**, *8*, 3991.
[33] D. N. Bowman, J. C. Asher, S. A. Fischer, C. J. Cramer, N. Govind, *Phys. Chem. Chem. Phys.* **2017**, *19*, 27452.
[34] A. Castro, H. Appel, M. Oliveira, C. A. Rozzi, X. Andrade, F. Lorenzen, M. A. Marques, E. Gross, A. Rubio, *Phys. Status Solidi B* **2006**, *243*, 2465.
[35] C. Brabec, U. Scherf, V. Dyakonov, *Organic Photovoltaics: Materials, Device Physics, and Manufacturing Technologies*, John Wiley & Sons, Hoboken, NJ **2011**.
[36] M. B. Smith, J. Michl, *Chem. Rev.* **2010**, *110*, 6891.
[37] B. Kumar, B. K. Kaushik, Y. S. Negi, *Polym. Rev.* **2014**, *54*, 33.
[38] N. Renaud, F. C. Grozema, *J. Phys. Chem.* **2015**, *6*, 360.
[39] L. Ma, K. Zhang, C. Kloc, H. Sun, C. Soci, M. E. Michel-Beyerle, G. G. Gurzadyan, *Phys. Rev. B* **2013**, *87*, 201203.
[40] N. Renaud, P. A. Sherratt, M. A. Ratner, *J. Phys. Chem.* **2013**, *4*, 1065.
[41] P. E. Teichen, J. D. Eaves, *J. Chem. Phys.* **2015**, *143*, 044118.
[42] C. Sutton, N. R. Tummala, D. Beljonne, J.-L. Brédas, *Chem. Mater.* **2017**, *29*, 2777.
[43] K. Bera, C. J. Douglas, R. R. Frontiera, *J. Phys. Chem.* **2017**, *8*, 5929.
[44] K. Bera, S. Y. Kwang, R. R. Frontiera, *J. Phys. Chem. C* **2020**, *124*, 25163.
[45] M. B. Smith, J. Michl, *Annu. Rev. Phys. Chem.* **2013**, *64*, 361.
[46] D. Casanova, *Chem. Rev.* **2018**, *118*, 7164.
[47] Y. Zhang, C.-H. Qi, N. Yamano, P. Wang, L.-J. Yu, Z.-Y. Wang-Otomo, J.-P. Zhang, *J. Phys. Chem.* **2022**, *13*, 3534.
[48] D. Manawadu, D. J. Valentine, M. Marcus, W. Barford, *J. Phys. Chem.* **2022**, *13*, 1344.
[49] A. Quaranta, A. Krieger-Liszkay, A. A. Pascal, F. Perreau, B. Robert, M. Vengris, M. J. Llansola-Portoles, *Phys. Chem. Chem. Phys.* **2021**, *23*, 4768.
[50] A. J. Musser, M. Maiuri, D. Brida, G. Cerullo, R. H. Friend, J. Clark, *J. Am. Chem. Soc.* **2015**, *137*, 5130.
[51] S. N. Sanders, E. Kumarasamy, A. B. Pun, M. L. Steigerwald, M. Y. Sfeir, L. M. Campos, *Chem* **2016**, *1*, 505.
[52] T. Hasobe, *Chem. Lett.* **2021**, *50*, 615.
[53] S. N. Sanders, E. Kumarasamy, A. B. Pun, K. Appavoo, M. L. Steigerwald, L. M. Campos, M. Y. Sfeir, *J. Am. Chem. Soc.* **2016**, *138*, 7289.
[54] L. J. Purvis, X. Gu, S. Ghosh, Z. Zhang, C. J. Cramer, C. J. Douglas, *J. Org. Chem.* **2018**, *83*, 1828.
[55] X. Gu, W. A. Luhman, E. Yagodkin, R. J. Holmes, C. J. Douglas, *Org. Lett.* **2012**, *14*, 1390.
[56] D. Dietze, R. A. Mathies, *ChemPhysChem* **2016**, *17*, 1224.
[57] T. Buckup, M. Motzkus, *Annu. Rev. Phys. Chem.* **2014**, *65*, 39.
[58] M. Kowalewski, B. P. Fingerhut, K. E. Dorfman, K. Bennett, S. Mukamel, *Chem. Rev.* **2017**, *19*, 12165.
[59] R. Berera, R. v. Grondelle, J. T. M. Kennis, *Photosynth. Res.* **2009**, *101*, 105.
[60] C. Fang, L. Tang, C. Chen, *J. Chem. Phys.* **2019**, *151*, 200901.

[61] K. Ramasesha, S. Leone, D. Neumark, *Annu. Rev. Phys. Chem.* **2016**, *67*, 41.
[62] J. J. Goings, J. M. Kasper, F. Egidi, S. Sun, X. Li, *J. Chem. Phys.* **2016**, *145*, 104107.
[63] T. S. Nguyen, J. Parkhill, *J. Chem. Theory Comput.* **2015**, *11*, 2918.
[64] A. Petrone, D. B. Lingerfelt, N. Rega, X. Li, *Phys. Chem. Chem. Phys.* **2014**, *16*, 24457.
[65] F. Perrella, X. Li, A. Petrone, N. Rega, *JACS Au* **2022**, *19*, 626.
[66] F. Perrella, A. Petrone, N. Rega, *J. Chem. Theory Comput.* **2023**, *3*, 70.
[67] F. Coppola, P. Cimino, F. Perrella, L. Crisci, A. Petrone, N. Rega, *J. Phys. Chem. A* **2022**, *126*, 7179.
[68] F. Coppola, P. Cimino, U. Raucci, M. G. Chiariello, A. Petrone, N. Rega, *Chem. Sci.* **2021**, *12*, 8058.
[69] M. G. Chiariello, U. Raucci, F. Coppola, N. Rega, *Phys. Chem. Chem. Phys.* **2019**, *21*, 3606.
[70] M. B. Oviedo, B. M. Wong, *J. Chem. Theory Comput.* **2016**, *12*, 1862.
[71] C. F. Negre, V. C. Fuertes, M. B. Oviedo, F. Y. Oliva, C. G. Sánchez, *J. Phys. Chem. C* **2012**, *116*, 14748.
[72] S. Meng, E. Kaxiras, *Nano Lett.* **2010**, *10*, 1238.
[73] Y. Takimoto, F. Vila, J. Rehr, *J. Chem. Phys.* **2007**, *127*, 154114.
[74] X. Li, S. M. Smith, A. N. Markevitch, D. A. Romanov, R. J. Levis, H. B. Schlegel, *Phys. Chem. Chem. Phys.* **2005**, *7*, 233.
[75] H. Eshuis, G. G. Balint-Kurti, F. R. Manby, *J. Chem. Phys.* **2008**, *128*, 114113.
[76] B. Gao, K. Ruud, Y. Luo, *J. Chem. Phys.* **2012**, *137*, 194307.
[77] C. T. Chapman, W. Liang, X. Li, *J. Phys. Chem.* **2011**, *2*, 1189.
[78] F. Ding, C. T. Chapman, W. Liang, X. Li, *J. Chem. Phys.* **2012**, *137*, 22A512.
[79] G. Donati, D. B. Lingerfelt, A. Petrone, N. Rega, X. Li, *J. Phys. Chem. A* **2016**, *120*, 7255.
[80] J. M. Kasper, P. J. Lestrange, T. F. Stetina, X. Li, *J. Chem. Theory Comput.* **2018**, *14*, 1998.
[81] A. Petrone, D. B. Williams-Young, S. Sun, T. F. Stetina, X. Li, *Eur. Phys. J. B* **2018**, *91*, 1.
[82] D. B. Williams-Young, A. Petrone, S. Sun, T. F. Stetina, P. Lestrange, C. E. Hoyer, D. R. Nascimento, L. Koulias, A. Wildman, J. Kasper, J. J. Goings, F. Ding, A. Eugene DePrince III, E. F. Valeev, X. Li, *Wiley Interdiscip. Rev.: Comput. Mol. Sci.* **2020**, *10*, e1436.
[83] A. D. Becke, *J. Chem. Phys.* **1993**, *98*, 5648.
[84] A. D. Becke, *Phys. Rev. A* **1988**, *38*, 3098.
[85] C. Lee, W. Yang, R. G. Parr, *Phys. Rev. B* **1988**, *37*, 785.
[86] B. Miehlich, A. Savin, H. Stoll, H. Preuss, *Chem. Phys. Lett.* **1989**, *157*, 200.
[87] A. D. Becke, *J. Chem. Phys.* **1993**, *98*, 1372.
[88] P. M. Gill, B. G. Johnson, J. A. Pople, M. J. Frisch, *Chem. Phys. Lett.* **1992**, *197*, 499.
[89] P. J. Stephens, F. J. Devlin, C. F. Chabalowski, M. J. Frisch, *J. Phys. Chem.* **1994**, *98*, 11623.
[90] N. Nakatani, S. Guo, *J. Chem. Phys.* **2017**, *146*, 094102.
[91] T. S. Haugland, E. Ronca, E. F. Kjønstad, A. Rubio, H. Koch, *Phys. Rev. X* **2020**, *10*, 041043.
[92] F. Coppola, M. Nucci, M. Marazzi, D. Rocca, M. Pastore, *ChemPhotoChem* **2023**, *7*, e202200214.
[93] M. Lewin, *J. Math. Chem.* **2008**, *44*, 967.
[94] J. Finley, P.-Å. Malmqvist, B. O. Roos, L. Serrano-Andrés, *Chem. Phys. Lett.* **1998**, *288*, 299.
[95] T. Helgaker, P. Jorgensen, J. Olsen, *Molecular Electronic-Structure Theory*, John Wiley & Sons, Hoboken, NJ **2013**.
[96] F. A. Evangelista, *J. Chem. Phys.* **2018**, *149*, 030901.
[97] F. Coppola, F. Perrella, A. Petrone, G. Donati, N. Rega, *Front. Mol. Biosci.* **2020**, *7*, 569990.
[98] R. Freitas, R. Rivelino, F. Mota, C. De Castilho, *J. Phys. Chem. A* **2011**, *115*, 12348.
[99] A. E. Mahdy, *Mol. Phys.* **2015**, *113*, 3531.
[100] J. González, I. Banos, I. León, J. Contreras-Garcia, E. Cocinero, A. Lesarri, J. Fernández, J. Millan, *J. Chem. Theory Comput.* **2016**, *12*, 523.
[101] T. Tsuzuki, S. Ogata, M. Uranagase, *Comput. Mater. Sci.* **2020**, *171*, 109281.
[102] G. Donati, A. Petrone, N. Rega, *Phys. Chem. Chem. Phys.* **2020**, *22*, 22645.
[103] U. Raucci, M. Savarese, C. Adamo, I. Ciofini, N. Rega, *J. Phys. Chem. B* **2015**, *119*, 2650.
[104] A. Petrone, P. Caruso, S. Tenuta, N. Rega, *Phys. Chem. Chem. Phys.* **2013**, *15*, 20536.
[105] Y. Zheng, B. M. Weight, A. C. Jones, V. Chandrasekaran, B. J. Gifford, S. Tretiak, S. K. Doorn, H. Htoon, *ACS Nano* **2021**, *15*, 923.
[106] C. M. Perez, D. Ghosh, O. Prezhdo, S. Tretiak, A. J. Neukirch, *J. Phys. Chem.* **2021**, *12*, 1005.
[107] P. Kim, A. J. Valentine, S. Roy, A. W. Mills, A. Chakraborty, F. N. Castellano, X. Li, L. X. Chen, *J. Phys. Chem.* **2021**, *12*, 6794.
[108] L. Lu, A. Wildman, A. J. Jenkins, L. Young, A. E. Clark, X. Li, *J. Phys. Chem.* **2020**, *11*, 9946.
[109] J. D. Leger, M. R. Friedfeld, R. A. Beck, J. D. Gaynor, A. Petrone, X. Li, B. M. Cossairt, M. Khalil, *J. Phys. Chem.* **2019**, *10*, 1833.
[110] M. J. Frisch, G. W. Trucks, H. B. Schlegel, G. E. Scuseria, M. A. Robb, J. R. Cheeseman, G. Scalmani, V. Barone, G. A. Petersson, H. Nakatsuji, X. Li, M. Caricato, A. V. Marenich, J. Bloino, B. G. Janesko, R. Gomperts, B. Mennucci, H. P. Hratchian, J. V. Ortiz, A. F. Izmaylov, J. L. Sonnenberg, D. Williams-Young, F. Ding, F. Lipparini, F. Egidi, J. Goings, B. Peng, A. Petrone, T. Henderson, D. Ranasinghe, V. G. Zakrzewski, J. Gao, N. Rega, G. Zheng, W. Liang, M. Hada, M. Ehara, K. Toyota, R. Fukuda, J. Hasegawa, M. Ishida, T. Nakajima, Y. Honda, O. Kitao, H. Nakai, T. Vreven, K. Throssell, J. A. Montgomery Jr., J. E. Peralta, F. Ogliaro, M. J. Bearpark, J. J. Heyd, E. N. Brothers, K. N. Kudin, V. N. Staroverov, T. A. Keith, R. Kobayashi, J. Normand, K. Raghavachari, A. P. Rendell, J. C. Burant, S. S. Iyengar, J. Tomasi, M. Cossi, J. M. Millam, M. Klene, C. Adamo, R. Cammi, J. W. Ochterski, R. L. Martin, K. Morokuma, O. Farkas, J. B. Foresman, D. J. Fox, *Gaussian1˜6 Revision C.01*, Gaussian Inc, Wallingford, CT **2016**.
[111] R. Kobayashi, R. D. Amos, *Chem. Phys. Lett.* **2006**, *420*, 106.
[112] Z.-L. Cai, M. J. Crossley, J. R. Reimers, R. Kobayashi, R. D. Amos, *J. Phys. Chem. B* **2006**, *110*, 15624.
[113] I. V. Rostov, R. D. Amos, R. Kobayashi, G. Scalmani, M. J. Frisch, *J. Phys. Chem. B* **2010**, *114*, 5547.
[114] R. Li, J. Zheng, D. G. Truhlar, *Phys. Chem. Chem. Phys.* **2010**, *12*, 12697.
[115] H. Li, R. Nieman, A. J. Aquino, H. Lischka, S. Tretiak, *J. Chem. Theory Comput.* **2014**, *10*, 3280.
[116] S. Kümmel, *Adv. Energy Mater.* **2017**, *7*, 1700440.
[117] N. Mardirossian, J. A. Parkhill, M. Head-Gordon, *Phys. Chem. Chem. Phys.* **2011**, *13*, 19325.
[118] A. D. Laurent, D. Jacquemin, *Int. J. Quantum Chem.* **2013**, *113*, 2019.
[119] R. Derian, K. Tokár, B. Somogyi, A. Gali, I. Štich, *J. Chem. Theory Comput.* **2017**, *13*, 6061.
[120] D. Jacquemin, A. Planchat, C. Adamo, B. Mennucci, *J. Chem. Theory Comput.* **2012**, *8*, 2359.
[121] M. Yamamura, A. Kuriyama, *Prog. Theor. Phys. Suppl.* **1987**, *93*, 1.
[122] G. Donati, D. B. Lingerfelt, C. M. Aikens, X. Li, *J. Phys. Chem. C* **2018**, *122*, 10621.
[123] M. J. Frisch, G. W. Trucks, H. B. Schlegel, G. E. Scuseria, M. A. Robb, J. R. Cheeseman, G. Scalmani, V. Barone, G. A. Petersson, H. Nakatsuji, X. Li, M. Caricato, A. V. Marenich, J. Bloino, B. G. Janesko, R. Gomperts, B. Mennucci, H. P. Hratchian, J. V. Ortiz, A. F.

Izmaylov, J. L. Sonnenberg, D. Williams-Young, F. Ding, F. Lipparini, F. Egidi, J. Goings, B. Peng, A. Petrone, T. Henderson, D. Ranasinghe, V. G. Zakrzewski, J. Gao, N. Rega, G. Zheng, W. Liang, M. Hada, M. Ehara, K. Toyota, R. Fukuda, J. Hasegawa, M. Ishida, T. Nakajima, Y. Honda, O. Kitao, H. Nakai, T. Vreven, K. Throssell, J. A. Montgomery Jr., J. E. Peralta, F. Ogliaro, M. J. Bearpark, J. J. Heyd, E. N. Brothers, K. N. Kudin, V. N. Staroverov, T. A. Keith, R. Kobayashi, J. Normand, K. Raghavachari, A. P. Rendell, J. C. Burant, S. S. Iyengar, J. Tomasi, M. Cossi, J. M. Millam, M. Klene, C. Adamo, R. Cammi, J. W. Ochterski, R. L. Martin, K. Morokuma, O. Farkas, J. B. Foresman, D. J. Fox, *Gaussian Development Version Revision J.02*, Gaussian Inc, Wallingford, CT **2019**.

[124] R. L. Martin, *J. Chem. Phys.* **2003**, *118*, 4775.

[125] J. M. Kasper, X. Li, *J. Comput. Chem.* **2020**, *41*, 1557.

[126] J. Xu, L. Zhu, D. Fang, B. Chen, L. Liu, L. Wang, W. Xu, *ChemPhysChem* **2012**, *13*, 3320.

SUPPORTING INFORMATION

Additional supporting information can be found online in the Supporting Information section at the end of this article.

How to cite this article: L. Crisci, F. Coppola, A. Petrone, N. Rega, *J. Comput. Chem.* **2024**, *45*(4), 210. https://doi.org/10.1002/jcc.27231